Three-dimensional simulation of viscous-flow agglomerate sintering

M. J. Kirchhof,[1] H.-J. Schmid,[2,*] and W. Peukert[3]
[1]*Department of Research and Development, Burgmann Industries GmbH & Co. KG, Äußere Sauerlacher Str. 6-10, 82515 Wolfratshausen, Germany*
[2]*Mechanical & Environmental Process Engineering, University of Paderborn, Pohlweg 55, 33098 Paderborn, Germany*
[3]*Institute of Particle Technology, Friedrich-Alexander University Erlangen-Nuremberg, Cauerstr. 4, 91058 Erlangen, Germany*
(Received 9 February 2009; revised manuscript received 5 July 2009; published 31 August 2009)

The viscous-flow sintering of different agglomerate particle morphologies is studied by three-dimensional computer simulations based on the concept of fractional volume of fluid. For a fundamental understanding of particle sintering characteristics, the neck growth kinetics in agglomerate chains and in doublets consisting of differently sized primary particles is investigated. Results show that different sintering contacts in agglomerates even during the first stages are not completely independent from each other, even though differences are small. The neck growth kinetics of differently sized primary particles is determined by the smaller one up to a size difference by a factor of approximately 2, whereas for larger size differences, the kinetics becomes faster. In particular, the agglomerate sintering kinetics is investigated for particle chains of different lengths and for different particle morphologies each having ten primary particles and nine initial sintering contacts. For agglomerate chains, the kinetics approximately can be normalized by using the radius of the fully coalesced sphere. In general, different agglomerate morphologies show equal kinetics during the first sintering stages, whereas during advanced stages, compact morphologies show significantly faster sintering progress than more open morphologies. Hence, the overall kinetics cannot be described by simply using constant morphology correction factors such as fractal dimension or mean coordination number which are used in common sintering models. However, for the first stages of viscous-flow agglomerate sintering, which are the most important for many particle processes, a sintering equation is presented. Although we use agglomerates consisting of spherical primary particles, our methodology can be applied to other aggregate geometries as well.

DOI: 10.1103/PhysRevE.80.026319 PACS number(s): 47.55.df, 81.20.Ev

I. INTRODUCTION

Surface-tension-driven sintering and coalescence of particle agglomerates and aggregates, respectively, are important in various fields such as aerosol processing of materials [1,2], rapid prototyping [3,4], emulsification [5], spray processing [6], atmospheric aerosol growth [7], green body sintering in materials engineering [8,9], sintering of hollow bodies including photonic fibers [10], and subcellular biology [11]. The fundamental physical mechanisms determining the sintering process itself are volume, surface and grain-boundary diffusion, evaporation and recondensation, and, as subject of this paper, viscous flow. For amorphous and vitreous materials, such as polymers (e.g., PMMA, HDPE, LDPE) and glasses (e.g., silica and mixed glasses) above glass transition temperature, viscous flow is supposed to be the predominant sintering mechanism [12,13]. The driving force for the process is the surface tension aiming to minimize the aggregate surface area.

The fundamental unit of agglomerate sintering in three dimensions (3D) is the sintering of two spheres and in two dimensions, the sintering of infinite cylinders. A first phenomenological model for the first stages of viscous-flow sintering of two spheres was initiated by Frenkel and Eshelby by equating the work of surface tension and the work of dissipation of mechanical energy due to viscous flow [14,15]. Hopper obtained an analytical exact expression for cylinders using complex variable theory for biharmonic functions [16,17]. Furthermore, various numerical approaches in two [18–21] and three [22–25] dimensions such as boundary element, finite element, and boundary integral methods have been reported dealing with the sintering of cylinders and doublets.

So far, some of the numerical methods mentioned above also have been used to study the sintering process of more than two primary particles. Martinez-Herrera and Derby investigated the sintering of axisymmetric particle configurations with up to three primary particles by a finite element method [26]. Comparing the sintering of doublets and three particle linear chains, they found that the overall relative shrinkage during the very first stages is nearly identical and for later stages that the three particle chains sinter at higher rates than the doublet. Zhou and Derby studied the sintering of three particles arranged by an angle of 90° [27] and arranged in a closed ring [28] also using a finite element method. They, for example, observed anisotropic shrinkage along different axes and inward rotation of the outer particles. Wakai *et al.* [29] conducted simulations of ideal sintering using Brakke's surface evolver program [30] and found out anisotropic shrinkage behavior during the sintering of four spheres arranged in a rhombus for different angles between the initial spheres. The reason for this behavior is that due to the different angles an additional particle contact arises at different times. Molecular dynamics simulations of linear particle chains [31] and L- and T-types [32], respectively, of Si nanoparticles resulting in a phenomenological model for these particle structures were conducted by Hawa and Zachariah.

*Author to whom correspondence should be addressed.

Koch and Friedlander introduced a constant rate law for the excess surface area decay [33]. Mathematically strict, the exponential model only is valid for the final sintering stages as shown by Friedlander and Wu [34]. In order to use the linear rate model also for larger aggregate structures, respectively, some extensions have been discussed. Johannessen *et al.* [35] introduced a model variant assuming the sintering rate of an agglomerate to be proportional to the number of primary particle contacts. Ulrich and Subramanian [36] developed a model, which later on has been refined by Lehtinen *et al.* [37], separating an aggregate into several units of primary particles and applying the linear rate law for each of these separated units. The number of primary particles in these units directly is correlated with the mean coordination number. However, Schmid *et al.* showed by computer simulations for gas-borne aggregates that unrealistic coordination numbers would have to be used to fit the described extension of the linear rate law to the simulation results [38,39].

The present work investigates morphological effects during viscous-flow sintering for completely different agglomerate particle structures. Our method is characterized by free modeling of the interface, adequate resolution of the surface curvature, and accurate surface area determination even for complex aggregate structures without any additional geometrical assumptions or *ad hoc* assumptions for the interface shape evolution. Examples for the relevance of sintering processes for structural evolution of particle aggregates during gas phase sintering are given in Refs. [39–41].

II. NUMERICAL METHODS

The viscous-flow sintering process is simulated solving the Navier-Stokes equations including free-surface movement by a fractional volume of fluid method [42]. The continuity and the momentum equations are used in the form $\partial\rho/\partial t+\nabla(\rho\mathbf{u})=0$ and $\partial\mathbf{u}/\partial t+(\mathbf{u}\nabla)\mathbf{u}=\mathbf{F}-1/\rho\nabla p+\eta/\rho\Delta\mathbf{u}$, with the velocity vector $\mathbf{u}$, the pressure p, the density ρ, the dynamic viscosity η, and the surface tension force $\mathbf{F}$ acting on a volume element. Considering isothermal flow, the energy equations can be neglected.

The particle surface is tracked by simultaneously solving a differential equation for the so-called volume fraction φ in each control volume surrounding each node of the grid. The volume fraction is defined by a function whose value is unity at nodes that are completely occupied by the particle phase and zero at nodes that are completely occupied by the gas phase. The particle interface is located where the volume fraction equals $\varphi=0.5$. In order to overcome the problems arising from a step function of the volume fraction φ at the particle interface, the interface is modeled by using the free continuous surface-tension model introduced by Brackbill *et al.* resulting in a continuous transition of the volume fraction function from unity to zero in the interface region [43]. Depending on the flow velocity and computational characteristics, the transition region consists of up to several mesh sizes. The model's strength is that the need for interface reconstruction is eliminated without imposing any restrictions to the complexity or dynamic evolution of the interface. Hence, as a major aspect of this work, the evolution of the interface can be computed without using any assumption for the interface shape during the process.

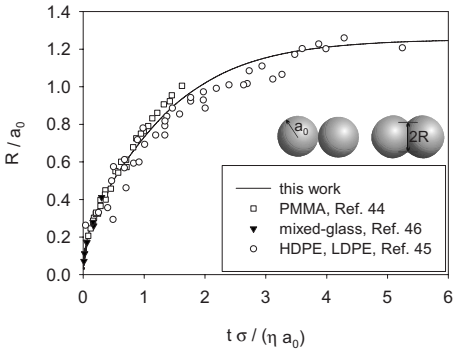

FIG. 1. Validation of the sintering system single sintering contacts. Evolution of the sintering neck size R/a_0 for doublets, first for the validated volume of fluid method and second for experimental data for different polymers and mixed glass (70% SiO_2).

The spatial discretization for the transient simulations is achieved by using an unstructured computational grid with tetrahedral mesh elements. Using a structured hexahedral mesh gives worse residual evolution in our case. Due to the overall curvature of the particle interface there are always mesh element faces forming small angles with the particle interface. The advantage of the tetrahedral mesh is that these elements are distributed over the particle interface whereas for the hexahedral mesh, there are complete regions having this restriction.

For a single sintering contact, i.e., a particle doublet, a careful mesh validation procedure was conducted decreasing mesh size that far that the simulation results do not change anymore. As a result, the validated mesh resolution is given by means of a mesh size density being some 250 000 elements per primary particle in our case. This mesh size density is applied for all particle morphologies. The time step undergoes a similar procedure for all morphologies.

The validated results for doublets are shown in Fig. 1 and are compared to experimental sintering data for polymers and glasses by means of the evolution of the relative sintering neck size R/a_0. The sintering time is given in dimensionless representation by $t\sigma/(\eta a_0)$, with the surface tension σ, the dynamic viscosity η, and the initial primary particle radius a_0. The simulations are in good agreement with the experimental kinetics results. Furthermore, our results have been compared to other numerical approaches (see Refs. [21–24]). These vary within approximately 30% depending on mesh resolution and sintering stage and our simulations agree within this range.

The present simulations are focused on the sintering of solid particles and therefore high viscosity ratios of disperse to continuous phase and small ratios of surface tension to dynamic viscosity are applied. However, the results can be adapted to droplets and bubbles as far as highly dynamic effects such as droplet splashing caused by high collision velocities are excluded. The methodology can be further applied to other geometries including fiber drawing, rapid prototyping, and solid free-form fabrication methods.

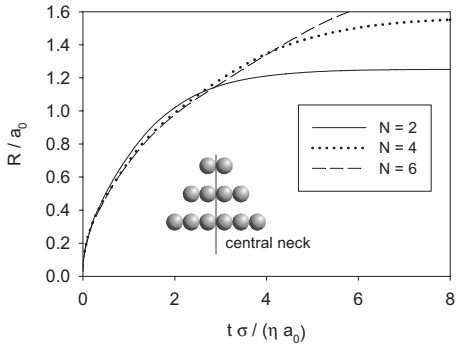

FIG. 2. Evolution of R/a_0 of the central neck within linear agglomerate chains of different lengths. For $N=2$, the neck size evolution differs slightly from the other two during the first stages, whereas for $N=4$ and $N=6$, the neck growth kinetics is nearly identical.

III. RESULTS AND DISCUSSION

This section is divided into four parts. Parts 1 and 2 deal with fundamental aspects of agglomerate sintering, namely, the mutual influence of different sintering contacts within agglomerates during neck growth and the sintering of differently sized primary particles. Third, morphology evolution during the sintering process of agglomerates is investigated. Fourth and final, a simple geometrical model is presented to discuss the influence of van der Waals interactions on the detected morphology effects. These interactions are supposed to play a major role in nanoparticle sintering.

A. Different sintering contacts in agglomerates

A major aspect of neck formation in agglomerates during the first sintering stages is whether or not single sintering contacts are independent from each other. Figure 2 shows the evolution of the sintering neck size R/a_0 of the central neck in agglomerate chains of different length, i.e., different number N of primary particles. The simulation results reveal that the evolution of the central neck even during the first stages ($R/a_0<1$) is not completely independent from N. The sintering neck of the doublet ($N=2$) in maximum shows a 6% faster sintering kinetics than agglomerate chains with $N\geq 4$. However, the kinetics nearly are identical for $N=4$ and $N=6$.

These differences may be explained in the following way. The particle material that flows into a specific sintering neck originates from the adjacent primary particles. For the doublet, each primary particle only has to "supply" one sintering neck. In contrary, for $N\geq 4$, the primary particle adjoining the central sintering neck additionally have to "supply" another sintering neck with particle material resulting for $N\geq 4$ in a slightly slower sintering kinetics than for the doublet. Comparing to that, the difference of the kinetics between $N=4$ and $N=6$ is negligible. Hence, the results reveal that the neck growth kinetics during the first stages slightly depends on the coordination number of the adjacent primary particles. Further investigations described below will show that there is no such obvious difference for the evolution of the agglomerate total surface area.

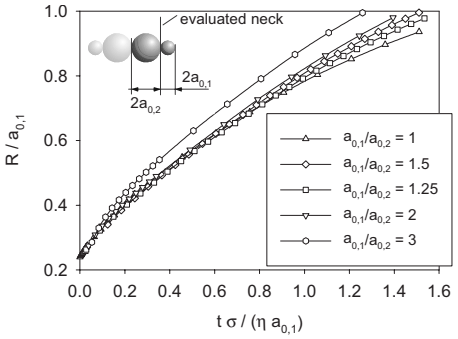

FIG. 3. Sintering neck size evolution for differently sized primary particles. Up to $a_{0,2}/a_{0,1}\approx 2$, the neck formation turns out to be completely dominated by the smaller primary particle.

B. Neck formation between differently sized primary particles

In particle dynamics, the collision kernel of differently sized particles increases with increasing particle size difference and sintering contacts formed in coagulation processes most often consist of differently sized primary particles. Hence, the neck formation process of differently sized primary particles is investigated.

In order to take further use of the three symmetry planes applied for our former simulations on doublet sintering [25], linear chains of four primary particles with two large primary particles in the middle and two small primary particles aside of them are modeled and the sintering neck between the primary particles of different size is evaluated. Figure 3 shows the neck growth kinetics $R/a_{0,1}$ for different primary particle radius quotients $a_{0,2}/a_{0,1}$ with $a_{0,1}$ always representing the smaller of the two primary particle radii. The neck growth kinetics for $R/a_{0,1}<0.7$ keeps in a range of $\pm 5\%$ for primary particle radius quotients $a_{0,2}/a_{0,1}\leq 2$. Only for $a_{0,2}/a_{0,1}=3$, the time to reach $R/a_{0,1}=0.7$ is faster by 30%. The reason for this behavior is supposed to be the unsymmetrical increase of the interface curvature on the side of the larger primary particle because with rising $a_{0,2}/a_{0,1}$, the sintering contact gets closer to the plane-sphere system. Hence, the viscous-flow sintering or maybe the sintering process in general is dominated by the smaller primary particle up to primary particle size differences by a factor of 2.

C. Effect of agglomerate morphology

1. Linear chains of different length

Linear agglomerate chains always consist of two primary particles at the ends each adjoining one sintering contact and several primary particles in the middle each adjoining two sintering contacts. Hence, the mean coordination number $\overline{N_K}$ of the N primary particles is $2-2/N$. Therefore, $\overline{N_K}$ equals twice the quotient of the number of sintering contacts and the number of primary particles $(N-1)/N$ asymptotically reaching a value of $\overline{N_K}=2$ for $N\rightarrow\infty$.

Figure 4 shows the sintering kinetics of agglomerate chains with $N\leq 10$ using four different normalizations of the sintering time in order to determine any possible characteristic correlation of the kinetics and the length of the agglomerate chains. All kinds of normalization show that for both

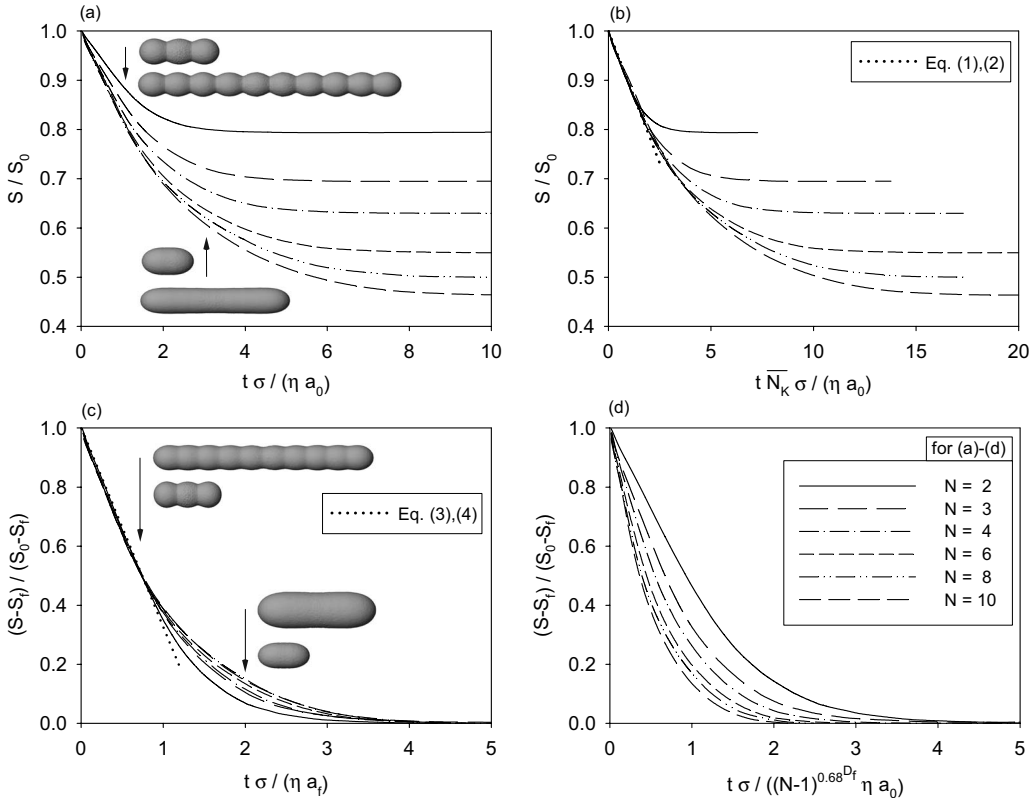

FIG. 4. Sintering kinetics of linear chains of different length N, depicted in different representations of the surface area evolution and of the dimensionless sintering time to determine general correlations (a)–(d). In (a) and (c), some sintering stages are shown for $N=3$ and $N=10$. In (b) and (c), first stage sintering Eqs. (1) and (3) are plotted.

doublets and larger agglomerates, the sintering rate is constant during the first stages. Hence, the overall sintering process of agglomerates only insufficiently can be described by an exponential function as used in the linear rate model by Koch and Friedlander [33]. Figure 4(a) depicts the evolution of the surface area by S/S_0, with the surface area S and the initial surface area S_0, as a function of the dimensionless sintering time $t\sigma/(\eta a_0)$. In addition to the numerical method described in Sec. II, a cross sectional integral method has been developed to accurately determine the surface area evolution.

The sintering rate is constant but different for each N during the first stages using this kind of surface representation. During the final stages, each surface evolution with monotonic decrease of the sintering rate asymptotically reaches its final value of $1/N^{1/3}$. In contrary, additionally applying $\overline{N_K}$ for the dimensionless sintering time as shown in Fig. 4(b), the sintering kinetics for all N is equal during the first stages.

In Fig. 4(c), the surface area evolution in reduced representation $(S-S_f)/(S_0-S_f)$ with the surface of the fully coalesced sphere S_f is plotted against a dimensionless sintering time using the radius of the fully coalesced sphere a_f instead of the initial primary particle radius a_0. For both Frenkel's [14,15] sintering law for the first stages and Koch and Friedlander's linear rate law, a_f is applied to determine the characteristic sintering time. Again, using this normalization of the sintering time, equal surface area evolution during the first stages is observed, although mathematically the linear rate law only has been proven for the final stages [34]. Instead, especially for sintering stages $(S-S_f)/(S_0-S_f)<0.5$, significant differences of the kinetics occur for different N reaching 35% in maximum [horizontally viewed in Fig. 4(c) for fixed $(S-S_f)/(S_0-S_f)$]. Note that the kinetics following the linear rate law of Koch and Friedlander would not show any difference of the kinetics if using a normalization of the sintering time by a_f as done in Fig. 4(c).

Using the normalizations in Figs. 4(b) and 4(c), the surface area evolution is independent from N during the first stages. Hence, the small dependency of the sintering neck growth kinetics on the coordination number as described in Sec. III A is too small to significantly affect the surface area evolution. Note that during the first stages, the evolution of the single sintering necks in the agglomerates cannot be determined from $(S-S_f)/(S_0-S_f)$ without N (see section below). Hence, the radius of the fully coalesced sphere has great influence on the first sintering stages although the single sintering necks are independent from each other concerning the surface area evolution.

In Fig. 4(d), a normalization for the simulation results is used basing on a phenomenological model for fractal agglomerates introduced by Hawa and Zachariah [31,32]. Conducting molecular-dynamics simulations for silicon resulted in the expression $t=t_{\mathrm{Frenkel}}(N-1)^{0.68^{D_f}}$ for the characteristic sintering time, with the fractal dimension D_f and the characteristic sintering time for doublets initiated by Frenkel. However, Hawa and Zachariah used a_0 instead of a_f for the determination of t_{Frenkel} as done by Frenkel himself.

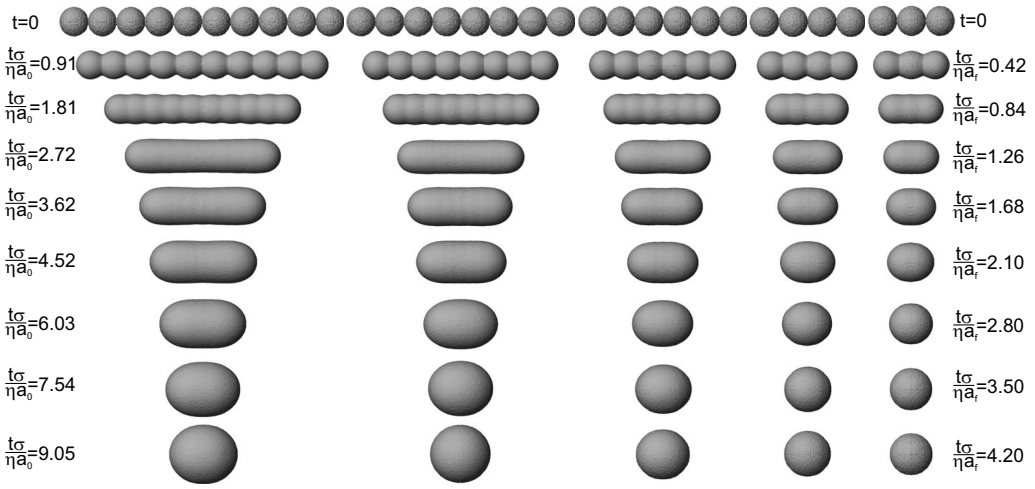

FIG. 5. Shape evolution of agglomerate chains with $N=3$, 4, 6, 8, and 10. For the dimensionless sintering times shown on the left, a_0 is used; on the right, a_f is used.

As shown in Fig. 4(d), the sintering kinetics significantly shifts to shorter $t\sigma/(N-1)^{0.68}$ ηa_0 (note that $D_f=1$ for agglomerate chains) with increasing N. Hence, the model of Hawa and Zachariah for $N\leq 10$ does not seem to be appropriate for a characteristic correlation between N and the sintering kinetics. However, it might be possible that the sintering curves fall together for sufficiently large N.

In Figs. 4(a) and 4(c), additionally the interface shape is shown for $N=3$ and $N=10$ each for two sintering stages in order to give an impression for the appearance at the specific stages. The complete shape evolution of the agglomerate chains is shown in Fig. 5. The shape evolution for the doublet can be found in Ref. [25]. In agreement with the discussion in Sec. III A, during the first stages, different sintering contacts can be considered to be independent from each other concerning the evolution of the surface area. Note that during the first stages, the correlation between surface area in reduced representation $(S-S_f)/(S_0-S_f)$ and sintering neck size R/a_0 of a single sintering contact changes with changing N, i.e., for $N>2$, the surface area state $(S-S_f)/(S_0-S_f)=0.5$ is not correlated with $R/a_0=0.7$ as for doublets but the single sintering necks already have proceeded further [see Fig. 4(c)].

For the linear chain with $N=10$, a special aspect concerning the shape evolution can be observed. After the end of the neck growth for sintering stages between $t\sigma/(\eta a_0)=2.72$ and $t\sigma/(\eta a_0)=4.52$ at the ends of the chain, a small thickening of the particle shape occurs. The cylindrical shape having two semispherical ends only can be seen starting at $t\sigma/(\eta a_0)=6.03$ before the shape develops versus the fully coalesced sphere. For $N=8$, this behavior only slightly is visible and for $N<8$, this behavior cannot be observed at all. In agreement with the results of Hawa and Zachariah [31,32], we conclude that such a shape thickening at the ends of agglomerate chains increases with increasing primary particle number N.

To sum up, the sintering kinetics of differently sized agglomerate chains cannot be normalized by a dimensionless sintering time. However, for $N\leq 10$, the normalization of the sintering time by the radius of the fully coalesced sphere a_f shows the best fitting. For the first stages, a general agglomerate sintering equation is presented below.

2. Different morphologies with constant N

In order to investigate the morphology effect separated from the effect of differing N of primary particles, sintering simulations for five different agglomerate morphologies are presented each having equal primary particle number $N=10$ and each having equal initial number of sintering contacts. Consequently, for the radius of the fully coalesced sphere a_f and the mean coordination number $\overline{N_K}$,

$$a_f=\sqrt[3]{10}a_0 \quad \text{and} \quad \overline{N_K}=1.8 \tag{1}$$

are valid for all these agglomerate morphologies. Hence, the different morphologies are characterized by the different coordination number distributions.

In Fig. 6, the shape evolution during the overall sintering process of the different morphologies is shown. The agglomerates comprise the following morphologies with radius of gyration R_G:

(a) Linear chain, $R_G=18.3a_0$,
(b) "Bone" structure, $R_G=15.8a_0$,
(c) "H" structure, $R_G=11.3a_0$,
(d) "X" structure, $R_G=11.1a_0$,
(e) "3D dumbbell" structure, $R_G=7.7a_0$.

All the initial structures have been selected so that no additional sintering contacts arise during the sintering process. Similar as for agglomerate chains, the overall evolution of the single sintering necks is uniform and independent from each other. However, after the end of neck growth stages large differences occur. For the densest (i.e., smallest R_G) morphology, the 3D dumbbell structure, full coalescence nearly is reached for a dimensionless sintering time of $t\sigma/(\eta a_0)=9.05$ against which for more open morphologies such as the linear chain and the "bone" structure, still a clear oval shape can be observed. Note that the sintering rate asymptotically reaches zero and therefore these differences during the finals stages are correlated with significant differences of the sintering kinetics.

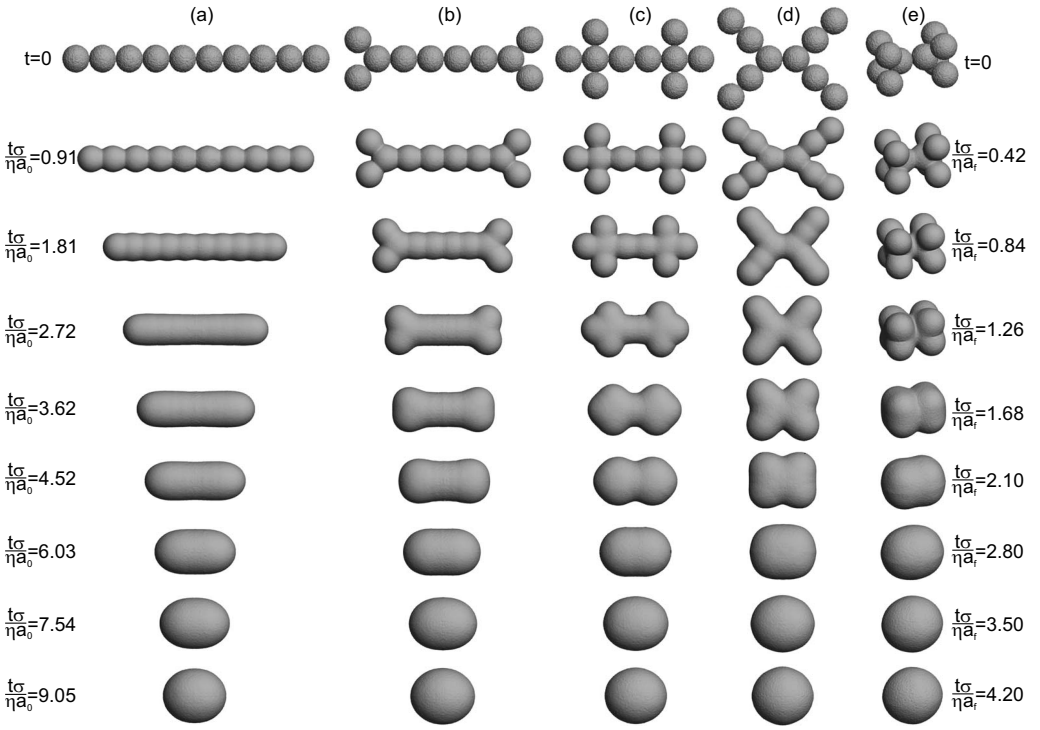

FIG. 6. Shape evolution of different agglomerate morphologies all being characterized by $N=10$ and $\overline{N_K}=1.8$. Structures shown are (a) linear chain, (b) bone structure, (c) H structure, (d) X structure, and (e) 3D-dumbbell structure. For the dimensionless sintering times shown on the left, a_0 is used; on the right, a_f is used.

In Fig. 7, the sintering kinetics by means of the surface area evolution of the different agglomerate morphologies is shown. Due to the fact that N, a_0, a_f, and $\overline{N_K}$ are equal for all morphologies, the above-discussed relative differences of the kinetics can be seen in every representation of the dimensionless sintering time. Hence, in Fig. 7, the results simply are shown as a function of $t\sigma/(\eta a_f)$. During the first stages, equal kinetics can be observed for all morphologies, again showing the quasi-independence of the single sintering contacts by means of the surface area evolution.

In contrary, during advanced stages for $(S-S_f)/(S_0-S_f)<0.5$, large differences occur. The H and the X structures show faster sintering progress than the linear chain whereas the kinetics of the bone structure only slightly differs from the latter one. The fastest kinetics is observed for the 3D Dumbbell structure showing a difference of sintering time [to reach equal $(S-S_f)/(S_0-S_f)$] in maximum by a factor of 1.6. During the sintering progress, the relative kinetics of the H and X structures reverses. At the beginning, the X structure shows a slower kinetics than the H structure before the order changes for $t\sigma/(\eta a_f)\approx 1.9$. Hence, a direct correlation between the different sintering kinetics and the different coordination number distributions of the primary particles within the agglomerates cannot be observed. For example, the bone structure and the X structure have equal numbers of coordination numbers, i.e., 4 times $N_K=1$, 4 times $N_K=2$, and 2 times $N_K=3$, but show very different sintering kinetics. Consequently, the absolute number of contacts and the spatial distribution of the specific coordination numbers play a major role.

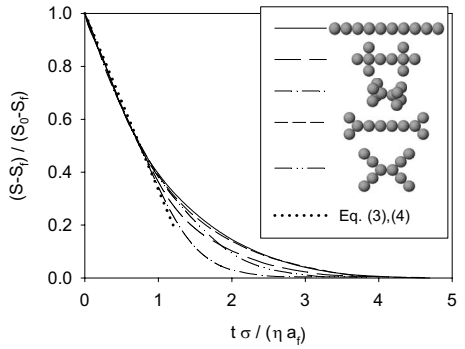

FIG. 7. Evolution of the surface area $(S-S_f)/(S_0-S_f)$ for different agglomerate morphologies with $N=10$ and $\overline{N_K}=1.8$.

Concluding, the sintering kinetics of different agglomerate morphologies having equal number of primary particles and initial sintering contacts is equal during the first sintering stages but differs significantly for advanced sintering stages with $(S-S_f)/(S_0-S_f)<0.5$. A simple normalization by using constant form factors as suggested by Hawa and Zachariah with the fractal dimension is not appropriate, at least for the agglomerate sizes discussed in this paper. However, the present results clearly show that during advanced sintering stages, denser agglomerate morphologies have a faster sintering kinetics than more open morphologies.

D. Agglomerate sintering equation

Summing up the simulation results described in Sec. III C, the viscous-flow sintering kinetics of agglomerates and aggregates, respectively, during the first stages can be ex-

pressed by the following sintering equations representing a constant sintering rate during the first stages:

$$\frac{d(S/S_0)}{dt} = -k_0 \frac{\overline{N_K}\sigma}{\eta a_0}, \tag{1a}$$

$$k_0 = 0.11, \tag{2}$$

or alternatively

$$\frac{d[(S-S_f)/(S_0-S_f)]}{dt} = -k_f \frac{\sigma}{\eta a_f}, \tag{3}$$

$$k_f = 0.67, \tag{4}$$

with the empirical constants k_0 and k_f, respectively. The sintering equations are shown in Figs. 4(b) and 4(c), respectively, and in Fig. 7. Note that the value of S/S_0 used in Eq. (1a) for the fully coalesced sphere depends on N, as does the value for the end of the first stages, e.g., $S_f/S_0 = 0.794$ for $N=2$ and $S_f/S_0 = 0.500$ for $N=8$. Nevertheless, the sintering rate $d(S/S_0)/dt$ can be expressed for all N as $-k_0\ \overline{N_K}\ \sigma/(\eta a_0)$.

Equation (1a) is valid for all N because it is proven by the present work that the mutual influence between different sintering contacts is negligible concerning the surface area evolution and the correlation between the number of primary particles N and the number of sintering contacts is represented mathematically correct by $\overline{N_K}$. The alternative sintering equation given in Eq. (3) is supposed to be valid for all N and here it is proven for at least $N \leq 10$.

E. Nanoparticle agglomerate sintering

Nanoparticles are of major importance in many fields including particle technology due to their extraordinary product properties [1]. For vitreous materials, the predominant sintering mechanism is supposed to be viscous flow, which is confirmed by experimental sintering studies for particles in the micrometer and millimeter regimes [44–46] and by comparing these experiments to our simulations for doublets (see Fig. 1). However, some of our current experimental work on nanoparticle sintering of silica show much shorter characteristic time scales than for macroscopic sintering. Hence, absolute sintering times for agglomerates will differ from the results of this paper. However, the question to be answered here is whether or not the present results for the morphological effects, i.e., different sintering behavior during advanced stages despite the equal sintering behavior during the first stages, also are valid for the nanometer-size regime. For nanoparticles, microscopic forces such as van der Waals interactions between the primary particles have to be considered during the first sintering stages. Computer simulations on nanoparticle sintering will be presented in a forthcoming publication. Van der Waals forces are known to be strong enough even to induce particle flattening of stiff materials without sintering, e.g., see JKR and DMT models [47,48].

Van der Waals interactions, in principle, do not only act between contacting but also between noncontacting primary particles. Hence, there might be an influence of noncontacting primary particles on the sintering of contacting primary particles. These aspects are discussed using the geometrical model shown by the inlet in Fig. 8. The van der Waals force between the noncontacting particles 1 and 3 is compared to the van der Waals force between particles 1 and 2 having the sintering contact. Following Hamaker, the interaction potential V_{att} between two equally sized spheres at surface distance d is [49]

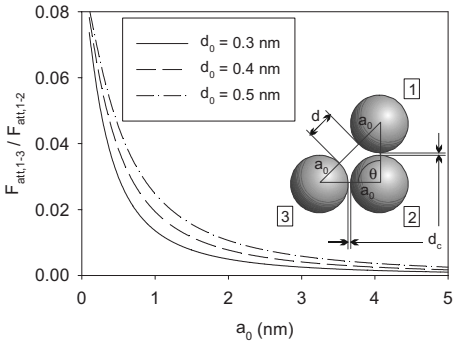

FIG. 8. Van der Waals force ratio $F_{att,1\text{-}3}/F_{att,1\text{-}2}$ between contacting and noncontacting primary particles depending on the primary particle radius a_0, shown for different assumptions for the contact distance d_c. Inset: Geometrical model for the calculation.

$$V_{att}(d) = -\frac{H}{6}\left[\frac{2a_0^2}{(d+2a_0)^2-4a_0^2} + \frac{2a_0^2}{(d+2a_0)^2} + \ln\left(1-\frac{4a_0^2}{(d+2a_0)^2}\right)\right], \tag{5}$$

with the Hamaker constant H. Consequently, the attractive force F_{att} is

$$F_{att}(d) = -\frac{dV_{att}(d)}{dd} = \frac{32a_0^6 H}{3(2a_0+d)^3(4a_0+d)^2 d^2}. \tag{6}$$

The surface distance d between particles 1 and 3 is a function of the primary particle radius a_0 and the contact distance d_c between the particles and results in $d=\sqrt{2}(2a_0+d_c)-2a_0$. The attractive force $F_{att,1\text{-}2}$ between the two contacting particles 1 and 2 is compared to the attractive van der Waals force $F_{att,1\text{-}3}$ between particles 1 and 3. Hence, the ratio of the two forces equals

$$\frac{F_{att,1\text{-}3}}{F_{att,1\text{-}2}} = \frac{d_c^2(4a_0+d_c)^2}{8\sqrt{2}(2a_0^2+4a_0d_c+d_c^2)^2}, \tag{7}$$

only depending on the primary particle radius a_0 and the contact distance d_c. Figure 8 shows the force ratio $F_{att,1\text{-}3}/F_{att,1\text{-}2}$ as a function of a_0 and d_c. The contact distance between flat spheres commonly is set to 0.4 nm [50], but to show its influence, the force ratio is plotted for different contact distances, i.e., 0.3, 0.4, and 0.5 nm, respectively.

For $a_0 \geq 1.3$, 1.7, and 2.1 nm, respectively, $F_{att,1\text{-}3}/F_{att,1\text{-}2}$ is less than 1%, indicating that van der Waals interactions of particle 3 on the sintering between particles 1 and 2 are negligible. Thus, for $a_0 > 2$ nm, van der Waals interactions as additional driving forces for the sintering process are limited to single sintering contacts. The given approximation may be

considered as conservative because typical agglomerate structures, e.g., formed in gas phase production processes, have mean coordination numbers slightly larger than 2, meaning that the angle between three primary particles usually is significantly larger than 90° and consequently van der Waals interactions between noncontacting primary particles are even smaller. However, it should be mentioned that the macroscopic simulation approach of this work only is valid as far as nanoparticles may be considered to form a continuum solid. To sum up, the morphological effects presented here are also valid for the nanometer-size regime, although the absolute sintering times for nanoparticles are supposed to differ due to van der Waals interactions.

IV. SUMMARY AND CONCLUSIONS

The viscous-flow agglomerate sintering process is studied by three-dimensional computer simulations based on the concept of fractional volume of fluid. Preliminary two fundamental aspects of sintering are investigated. First result is that different sintering necks are not completely independent from each other even during the first sintering stages, i.e., during neck formation. It is supposed that the kinetics of a specific neck depends on whether or not the adjoining primary particles additionally have to supply other sintering necks with particle material, i.e., there is a dependency on the coordination number. However, the differences of the neck growth kinetics are small and the differences concerning the most important sintering measurement, the surface area evolution, are negligible. Second, the neck formation kinetics of differently sized particles is investigated showing that up to a size difference by a factor of approximately 2, the sintering neck formation is completely dominated by the smaller primary particle.

The influence of morphology on the kinetics is studied simulating the sintering of, first, agglomerate chains of different lengths and, second, different agglomerate structures each having equal number of primary particles and initial sintering contacts. It turns out that the overall kinetics cannot be normalized by a dimensionless sintering time. However, for the first stages, a sintering equation can be presented because the different sintering contacts are nearly independent from each other. The first stages are characterized by a constant sintering rate of the surface area reduction.

Especially, the sintering of different morphologies all having ten primary particles shows that the overall kinetics of the process cannot be described by using constant form factors such as the fractal dimension or the mean coordination number. During the first stages, the surface area reduction is equal for all morphologies, whereas during advanced stages, large differences occur. During these advanced stages, in principal, dense particle morphologies show faster sintering kinetics than more open structures.

The absolute sintering times achieved by the present macroscopic approach are supposed to be valid for primary particle sizes larger than some hundred nanometers. For ultrafine particles, van der Waals interactions between primary particles have major influence on sintering. Thus, a simple geometrical model is presented to study the influence of van der Waals interactions between contacting and noncontacting primary particles. For primary particle radii larger than approximately 2 nm, van der Waals interactions between noncontacting primary particles turn out to be negligible. Hence, the morphological effects determined in this paper also can be assigned to the nanometer-size range.

[1] F. E. Kruis, H. Fissan, and A. Peled, J. Aerosol Sci. **29**, 511 (1998).

[2] T. T. Kodas and M. Hampden-Smith, *Aerosol Processing of Materials* (Wiley-VCH, New York, 1999).

[3] H. H. Zhu, L. Lu, and J. Y. H. Fhu, Mater. Sci. Eng., A **371**, 170 (2004).

[4] G. Casalino, L. A. C. De Filippis, A. D. Ludovico, and L. Tricarico, J. Laser Appl. **14**, 100 (2002).

[5] J.-C. Lepers, B. D. Favis, and C. Lacroix, J. Polym. Sci., Part B: Polym. Phys. **37**, 939 (1999).

[6] L. Mädler, H. Kammler, R. Müller, and S. E. Pratsinis, J. Aerosol Sci. **33**, 369 (2002).

[7] M. Kulmala, H. Vehkamäki, T. Petäjä, M. Dal Maso, A. Lauri, V.-M. Kerminen, W. Birmili, and P. H. McMurry, J. Aerosol Sci. **35**, 143 (2004).

[8] W. Schatt, *Sintervorgänge* (VDI, Düsseldorf, 1992).

[9] M. F. Ashby, Acta Metall. **22**, 275 (1974).

[10] M. B. MacChesney, D. W. Johnson, Jr., S. Bhandarkar, M. P. Bohrer, J. W. Fleming, E. M. Monberg, and D. J. Trevor, J. Non-Cryst. Solids **226**, 232 (1998).

[11] G. Poste and A. C. Allison, Biochim. Biophys. Acta **300**, 421 (1973).

[12] G. C. Kuczynski, *Sintering Processes* (Plenum Press, New York, 1980).

[13] G. C. Kuczynski, J. Appl. Phys. **20**, 1160 (1949).

[14] J. Frenkel, J. Phys. (USSR) **9**, 385 (1945).

[15] J. D. Eshelby, Trans. AIME **185**, 806 (1949).

[16] R. W. Hopper, J. Am. Ceram. Soc. **67**, C262 (1984); see also errata, **68**, C138 (1985) and Ref. [12] in this paper.

[17] R. W. Hopper, J. Fluid Mech. **213**, 349 (1990).

[18] H. K. Kuiken, J. Fluid Mech. **214**, 503 (1990).

[19] G. A. L. van de Vorst, M. M. Mattheij, and H. K. Kuiken, J. Comput. Phys. **100**, 50 (1992).

[20] J. W. Ross, W. A. Miller, and G. C. Weatherly, J. Appl. Phys. **52**, 3884 (1981).

[21] J. I. Martinez-Herrera and J. J. Derby, AIChE J. **40**, 1794 (1994).

[22] A. Jagota and P. R. Dawson, J. Am. Ceram. Soc. **73**, 173 (1990).

[23] Y. Hiram and A. Nir, J. Colloid Interface Sci. **95**, 462 (1983).

[24] R. S. Garabedian and J. J. Helble, J. Colloid Interface Sci. **234**, 248 (2001).

[25] V. Yadha and J. J. Helble, J. Aerosol Sci. **35**, 665 (2004).

[26] J. I. Martinez-Herrera and J. J. Derby, J. Am. Ceram. Soc. **78**,

645 (1995).
[27] H. Zhou and J. J. Derby, J. Am. Ceram. Soc. **81**, 533 (1998).
[28] H. Zhou and J. J. Derby, Int. J. Numer. Methods Fluids **36**, 841 (2001).
[29] F. Wakai, K. Chihara, and M. Yoshida, Acta Mater. **55**, 4553 (2007).
[30] K. A. Brakke, Exp. Math. **1**, 141 (1992).
[31] T. Hawa and M. R. Zachariah, Phys. Rev. B **76**, 054109 (2007).
[32] T. Hawa and M. R. Zachariah, J. Aerosol Sci. **38**, 793 (2007).
[33] W. Koch and S. K. Friedlander, J. Colloid Interface Sci. **140**, 419 (1990).
[34] S. K. Friedlander and M. K. Wu, Phys. Rev. B **49**, 3622 (1994).
[35] T. Johannessen, S. E. Pratsinis, and H. Livbjerg, Chem. Eng. Sci. **55**, 177 (2000).
[36] G. D. Ulrich and N. S. Subramanian, Combust. Sci. Technol. **17**, 119 (1977).
[37] K. E. J. Lehtinen, R. S. Windeler, and S. K. Friedlander, J. Colloid Interface Sci. **182**, 606 (1996).
[38] H.-J. Schmid, S. Tejwani, C. Artelt, and W. Peukert, J. Nanopart. Res. **6**, 613 (2004).
[39] H.-J. Schmid, B. Al-Zaitone, C. Artelt, and W. Peukert, Chem. Eng. Sci. **61**, 293 (2006).
[40] C. Artelt, H.-J. Schmid, and W. Peukert, Chem. Eng. Sci. **61**, 18 (2006).
[41] C. Artelt, H.-J. Schmid, and W. Peukert, J. Aerosol Sci. **36**, 147 (2005).
[42] C. W. Hirt and B. D. Nichols, J. Comput. Phys. **39**, 201 (1981).
[43] J. U. Brackbill, D. B. Kothe, and C. Zemach, J. Comput. Phys. **100**, 335 (1992).
[44] N. Rosenzweig and M. Narkis, Polym. Eng. Sci. **21**, 1167 (1981).
[45] C. T. Bellehumeur, M. K. Bisaria, and J. Vlachopoulos, Polym. Eng. Sci. **36**, 2198 (1996).
[46] W. D. Kingery and M. Berg, J. Appl. Phys. **26**, 1205 (1955).
[47] K. L. Johnson, K. Kendall, and A. D. Roberts, Proc. R. Soc. London, Ser. A **324**, 301 (1971).
[48] B. V. Derjaguin, V. M. Muller, and Y. P. Toporov, J. Colloid Interface Sci. **53**, 314 (1975).
[49] H. C. Hamaker, Physica D **10**, 1058 (1937).
[50] J. N. Israelachvilli, *Intermolecular and Surface Forces* (Academic Press, London, 1992).